





## Crystal mush dykes as conduits for mineralising fluids in the Yerington porphyry copper district, Nevada

Lawrence C. Carter <sup>1✉</sup>, Ben J. Williamson <sup>1,2</sup>, Simon R. Tapster <sup>3</sup>, Catia Costa<sup>4</sup>, Geoffrey W. Grime <sup>4</sup> & Gavyn K. Rollinson<sup>1</sup>

Porphyry-type deposits are the world's main source of copper and molybdenum and provide a large proportion of gold and other metals. However, the mechanism by which mineralising fluids are extracted from source magmas and transported upwards into the ore-forming environment is not clearly understood. Here we use field, micro-textural and geochemical techniques to investigate field relationships and samples from a circa 8 km deep cross-section through the archetypal Yerington porphyry district, Nevada. We identify an interconnected network of relatively low-temperature hydrothermal quartz that is connected to mineralised miarolitic cavities within aplite dykes. We propose that porphyry-deposit-forming fluids migrated from evolved, more water-rich internal regions of the underlying Luhr Hill granite via these aplite dykes which contained a permeable magmatic crystal mush of feldspar and quartz. The textures we describe provide petrographic evidence for the transport of fluids through crystal mush dykes. We suggest that this process should be considered in future models for the formation of porphyry- and similar-type deposits.

<sup>1</sup>Camborne School of Mines, University of Exeter, Cornwall, UK. <sup>2</sup>Natural History Museum, London, UK. <sup>3</sup>British Geological Survey, Nottingham, UK. <sup>4</sup>University of Surrey Ion Beam Centre, Guildford, UK. ✉email: [l.c.carter@exeter.ac.uk](mailto:l.c.carter@exeter.ac.uk)

Porphyry deposit-forming fluids are derived from large, long-lived magmatic systems<sup>1–3</sup> where melt or mush reservoirs are at depths of between around 5 to 15 km<sup>4,5</sup> or in more extensive transcrustal magmatic systems e.g.<sup>6–8</sup>. How ore-forming fluids are transported from these reservoirs and focused into narrow, relatively shallow (ca. 2–5 km deep<sup>5,9</sup>), zones of economic mineralisation<sup>5,10–13</sup> is an important yet missing link in our understanding of porphyry deposit formation<sup>5,14</sup>. Existing models commonly invoke: convection of bubble-rich magma in upper crustal magma chambers and upwards emplacement to form porphyritic stocks and dykes e.g.<sup>4,15–17</sup>; accumulation of volatile-saturated melts in cupolas which act as exhaust valves episodically ejecting fluids and magma by repeated dyke injections e.g.,<sup>5,14,18</sup>; or through sustaining brittle fracture networks<sup>11</sup>. These generic concepts are still debated as there is a paucity of observational evidence for a critical link to porphyry ore genesis. Although field observations from across magmatic systems potentially offer snapshots of the complex sequence of dynamic processes that lead to fluid extraction<sup>19</sup>, most are limited due to a lack of vertically extensive exposure<sup>10</sup>. One of the main exceptions to this is the archetypal Yerington porphyry system, Nevada, which has been tilted to reveal a vertical section from palaeosurface to a depth of ca. 8 km<sup>14</sup>. This has therefore provided important constraints for porphyry deposit models e.g.<sup>4,5,12,20,21</sup>, including computational simulations of the thermal evolution of magmatic systems and ore fluid focusing<sup>11,22</sup>. Despite having such examples, evidence as to how the fluids are transported upwards has been circumstantial, largely based on the spatial proximity of the ore zone to the cupola and porphyry dykes. Understanding this fluid transport step is vital for developing more reliable porphyry exploration models and may give clues as to why very few known porphyry-type magmatic systems are economically mineralised.

The section through the Yerington District has exposed surface volcanics, three major plutons, hundreds of dykes and four known porphyry deposits (Fig. 1). The plutons are the McLeod Hill quartz monzodiorite, Bear quartz monzonite and Luhr Hill granite (Fig. 1), in order of decreasing age and volume, and increasing emplacement

depth and silica content<sup>14</sup>. Cross-cutting these, but focused mainly by the structure of the apophyses of the Luhr Hill granite, are granite-composition porphyry and aplite dykes. These are also concentrated in the areas of the four known porphyry copper deposits: Ann Mason, Yerington, MacArthur and Bear<sup>23–26</sup>.

## Results and discussion

From existing conceptual models for the Yerington District e.g.<sup>14,22</sup>, and more generalised schemes for porphyry deposits e.g.<sup>4,5,12,17,20,21</sup>, which are mostly based on spatial relations, petrographic studies and geochemistry, the porphyry dykes and mineralising fluids are likely to have emanated from the spatially associated cupolas and upper regions (~3–6 km depth) of the Luhr Hill granite<sup>14</sup>. However, from our first-order field observations that span the entire cupola and upper regions of the Luhr Hill granite, where exposed, we could find no definitive textural evidence (e.g., miarolitic cavities<sup>27</sup> or directly sourced quartz or other veins) for fluid exsolution from the granite or porphyry dykes in these regions. Contacts between the granite cupola and precursor McLeod Hill quartz monzodiorite were sharp with no metasomatic effects beyond the otherwise later, pervasive, mostly sodic-calcic and propylitic porphyry-related alteration<sup>5</sup>.

The granite cupolas do however contain rare isolated quartz-feldspar pegmatitic orbs and massive silica bodies (nomenclature after<sup>28</sup>) (Fig. 2; Supplementary Fig. 1). These can be likened to orbicules and other spheroidal textures, found in a wide variety of magmatic rocks, whose origins are poorly understood but which are widely thought to crystallise from pockets of exsolved aqueous fluid e.g.<sup>29–32</sup>. However, from a combination of features, the pegmatitic orbs in the Luhr Hill granite are almost certainly magmatic in origin (i.e., crystallised from a silicate melt): they have an almost entirely anhydrous mineralogy (quartz, K-feldspar, plagioclase, accessory titanite and Fe-oxides, with only trace biotite), they are unmineralised, lack concentric shells and a central nucleation point (usual in orbicules<sup>29–31</sup>), have no cavities (once fluid-filled, i.e., they are not miarolitic cavities), are not connected to or associated with veins (i.e., there are no fluid escape

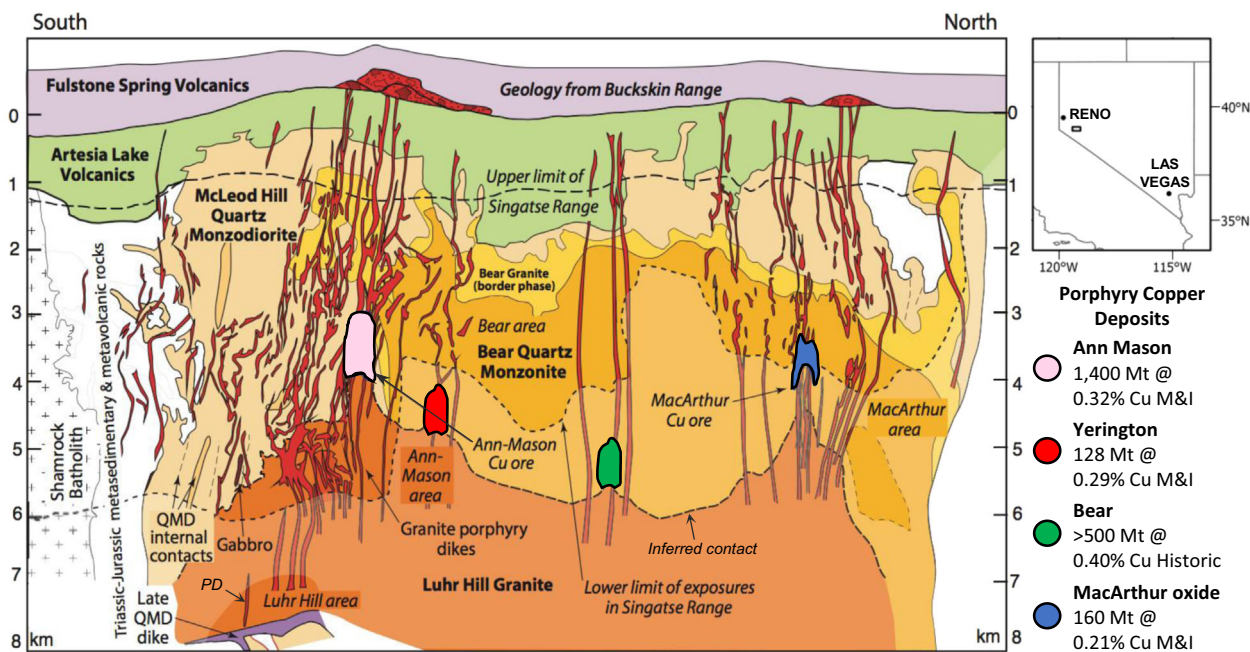


**Fig. 1** Pre-tilt cross-section through the Yerington porphyry copper district, Nevada. Reconstructed to a palaeo-depth of 8 km, showing the intrusive units of the Jurassic Yerington batholith, the various generations of porphyry dyke swarms which were focussed through apophyses of the Luhr Hill granite, the district's four known porphyry copper deposits and overlying volcanics. QMD = quartz monzodiorite. Porphyry dyke (PD) in Supplementary Fig. 3. Modified after<sup>14,22</sup>. Resource estimates<sup>23–26</sup>. M&I = measured & indicated, historic = non-compliant historic estimate.

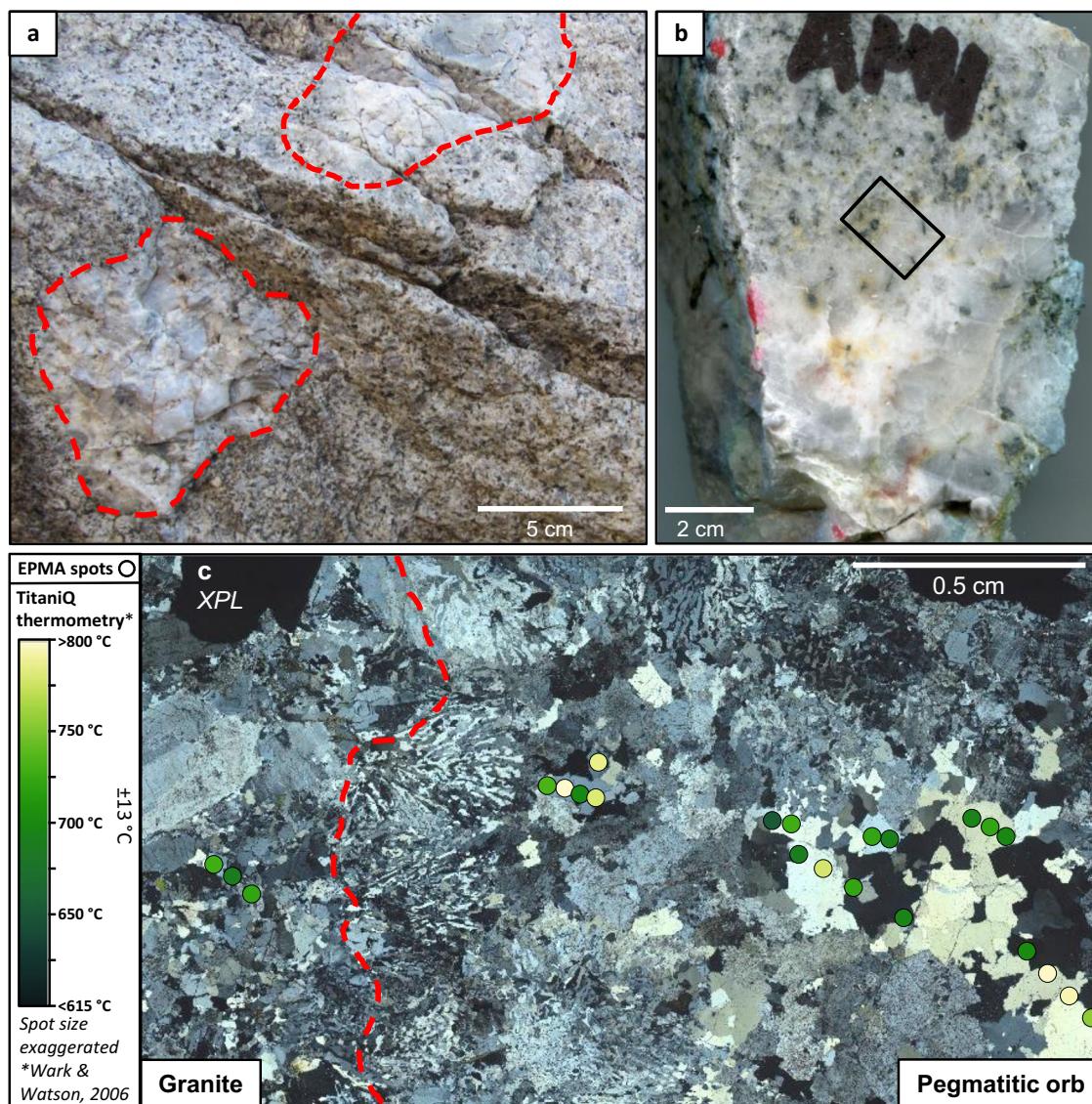


**Fig. 2** Quartz-feldspar pegmatitic orbs in the Luhr Hill granite cupola. **a, b** Field and sample photograph of quartz-feldspar pegmatitic orbs (outlined by red dashed lines) in the exposed cupola of the Luhr Hill granite, palaeo-vertically below the Ann Mason porphyry deposit<sup>14</sup>; **c** Photomicrograph under cross polarised light (XPL, location in **b**), showing micro-graphic texture at the margins of the pegmatitic orb (red dashed line), suggesting inward crystallisation, and locations of EPMA spot analyses for TitaniQ thermometry<sup>39</sup> (Circles coloured as per legend).

textures) or adjacent alteration, show no evidence of collapse as a result of fluid loss, grew inwards and show marginal micrographic textures (Fig. 2). Some spheroids with anhydrous mineralogies are thought to form as a result of H<sub>2</sub>O saturation in basaltic melts, e.g., in the Troodos, however, these do not show inward growth or graphic textures and are often accompanied by fluid-escape textures and/or alteration<sup>32</sup>. The micrographic intergrowths seen in the pegmatitic orbs could be interpreted as indicating near volatile-saturated conditions in the magmas e.g.<sup>33</sup>, a wider range of water activities<sup>34</sup> or, based on experimental work, that the melts were at least water rich (~4 wt% water<sup>35</sup>). Alternatively, from experimental work at significant H<sub>2</sub>O concentrations, graphic and spherulitic quartz-feldspar intergrowths can be produced by undercooling<sup>36</sup>. It has also been demonstrated that pegmatitic and graphic textures require undercooling but not water saturation for their formation e.g.<sup>37,38</sup> and could form from highly undercooled, relatively viscous, flux poor and therefore water undersaturated magmas<sup>27,34</sup>. Further evidence to support a magmatic origin for the Luhr Hill granite's orbs is that their mean TitaniQ<sup>39</sup>

crystallisation temperatures (using Ti-in-quartz measured by electron probe microanalysis [EPMA]) of 736 °C ( $n = 29$ ) is comparable to a mean of 727 °C ( $n = 20$ ) for magmatic quartz in the host Luhr Hill granite (see Supplementary Data 1). In summary, we interpret that, whilst highly undercooled, the cupola itself was unlikely to have been the direct source of mineralising fluids. Further, even if the pegmatitic orbs and massive silica bodies do represent pockets of exsolved fluids, given their isolation and rarity, we suggest that the volume of fluid escaping as a result of their crystallisation was minimal. We therefore propose that the cupola was not the source of mineralising fluids but that these migrated via dykes from deeper, more evolved portions of the Luhr Hill granite<sup>14</sup>.

Aplite dykes in the Yerington District occur pervasively from below to within the Ann Mason and Yerington porphyry deposits. These are numerous in number, with local occurrence of several dykes per metre (Supplementary Fig. 2), they cross-cut the cupolas and the apparent deepest exposures of the Luhr Hill granite (7–8 km<sup>14</sup>) (Supplementary Fig. 3). As such, their source

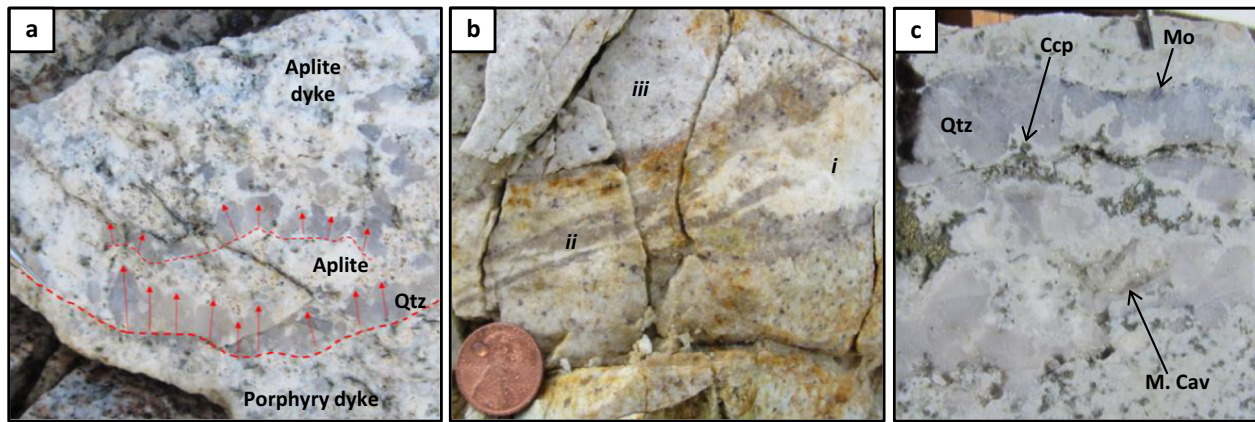


**Fig. 3 Magmatic-hydrothermal textures in aplite dykes.** **a** Field photograph from the exposed cupola of the Luhr Hill granite showing quartz (Qtz) unidirectional solidification textures (USTs) (red arrows marking c-axes) in an aplite dyke, indicating rapid pressure fluctuations<sup>28</sup> or likely first-type boiling during dyke emplacement<sup>40</sup>. Pencil tip for scale; **b** Field photograph from within the Yerington Mine (Yerington porphyry deposit) of interfingering aplite dyke (i) and quartz selvages (ii). The dyke is hosted within a slighter coarser-grained aplite dyke (iii). This is suggestive that the aplite magma was co-eval with a magmatic-hydrothermal fluid which crystallised quartz. Coin for scale; **c** Photograph of drill core from the Ann Mason porphyry deposit showing a pegmatitic selvage in an aplite dyke which cross-cuts the Luhr Hill granite. The pegmatite shows quartz USTs growing inwards from its rim, molybdenite (Mo) along its margins, a miarolitic cavity (M. Cav) and paragenetically late hypogene chalcopyrite (Ccp) which appears to be interstitial or to have precipitated within open spaces, probably also miarolitic cavities. Pencil tip for scale.

is therefore likely to be deeper unexposed parts of the Luhr Hill granite. Multiple generations of aplites are seen to have complex cross-cutting relations but locally they mingle with magmas which formed the porphyritic dykes (Supplementary Fig. 4) and are also cross-cut by mineralised veins (Supplementary Fig. 5). At least some aplite dykes were therefore contemporaneous with, yet distinct from the porphyry dykes, and were early- to syn-mineralisation. The presence of rare unidirectional solidification textures (USTs) (Fig. 3a & c) within aplites injected into the Luhr Hill granite is likely to indicate rapid pressure fluctuations<sup>28</sup> and probable fluid exsolution via ‘first-type’ boiling<sup>40</sup>. Interfingering aplite and quartz selvages (Fig. 3b) and common miarolitic cavities, where euhedral crystals grew into once fluid-filled spaces (Figs. 3c and 4), indicate the aplites’ formation at the magmatic-hydrothermal transition. Previous work in Yerington and other porphyry districts suggests that aplitic and/or pegmatitic magmas likely contributed to hydrothermal alteration e.g.<sup>41–43</sup>, but they have not previously been linked to substantive hypogene mineralisation. From our observations they are often mineralised, hosting pegmatitic segregations, sulfide-bearing miarolitic cavities and early A- and B-type veins (nomenclature after<sup>44</sup>) which locally terminate at the dyke margins (Figs. 3 and 4).

On a tens of micron scale, from detailed scanning electron microscopy with energy dispersive X-ray analysis (SEM-EDX) and cathodoluminescence (CL) imaging (Fig. 5; Supplementary Figs. 6–10), aplite dykes contain a wormy quartz texture throughout their groundmass comprising of polycrystalline branching, highly interconnected generations of quartz (moderate to dark CL response, ‘Qtz ii & iii’ in Fig. 5b–d), in addition to discrete magmatic quartz grains (brighter CL response, ‘Qtz i’ in Fig. 5b–d). The aplites’ wormy texture, which can be continuously traced in 2D across entire thin sections (e.g., Fig. 5a), indicates very high orders of connectivity in 3D, akin to descriptions of interconnected miarolitic cavities<sup>45</sup> and continuous chains of minerals that trace migration routes during melt extraction<sup>19</sup>. We interpret this wormy texture as marking an interconnected pathway for magmatic-hydrothermal fluids through inter-crystal spaces in a mush, the latter term referring to a continuous crystal framework<sup>6</sup>. It is already accepted that extensive porosity can exist within mechanically coherent frameworks of tabular silicate

minerals with crystal fractions as high as  $\sim 0.75$ <sup>46</sup>. Further, it has been experimentally demonstrated that melt extraction from cooling mushes increases close to their solidus and operates efficiently at crystal fractions of 0.6–0.93<sup>19</sup>.

An alternative explanation for the wormy quartz/feldspar fabric in the aplites is that it is a symplectitic texture, i.e., an intergrowth of minerals that crystallised simultaneously<sup>47</sup>, formed, for example, as a result of rapid depressurization and crystallisation of the aplitic groundmass. For a number of reasons this is deemed unlikely: (a) Paragenetic relations suggest albite crystallised earlier or coevally with K-feldspar, evidenced from the presence of albite inclusions in K-feldspar, but very few K-feldspar inclusions in albite; whereas quartz crystallised relatively late as there are very few quartz inclusions in the albite and K-feldspar. Rare examples of quartz inclusions within K-feldspar, which have the same CL response as discrete grains in the groundmass, are possibly due to 3-D interfingering of these phases rather than their presence as inclusions (Fig. 5b; Supplementary Figs. 7–10). From QEMSCAN mineral associations data (defined as mineral/pixel adjacency, or the percentage of one mineral touching another in a sample), albite is more associated in time with K-feldspar than quartz (see Supplementary Data 2); (b) The aplite contains multiple generations of quartz, identifiable from CL images and from varying titanium concentrations, with lower temperature quartz (‘Qtz ii & iii’) forming a network around higher temperature quartz (‘Qtz i’), albite and K-feldspar (Fig. 5b–d; Supplementary Fig. 7); (c) The branching quartz generations (‘Qtz ii & iii’) appear to join the clearly zoned early hydrothermal quartz in the miarolitic cavity, having the same CL response, Ti concentrations and range of Titanium<sup>39</sup> temperatures (from EPMA and Total Ion Beam Analysis [Total-IBA]) (‘Qtz ii & iii’ in Fig. 5b–d and 6; see Supplementary Data 1), and they are therefore likely to have crystallised contemporaneously and from the same fluid. This fluid was almost certainly aqueous rather than a silicate melt as the miarolitic cavity clearly represents a pocket of exsolved hydrothermal fluid (as per models for their formation<sup>27</sup>) which crystallised a non-magmatic association of quartz and then quartz and chalcopyrite simultaneously (from the presence of chalcopyrite inclusions in late quartz overgrowths, Fig. 5b; Supplementary Figs. 8–10). From these mineral relations,

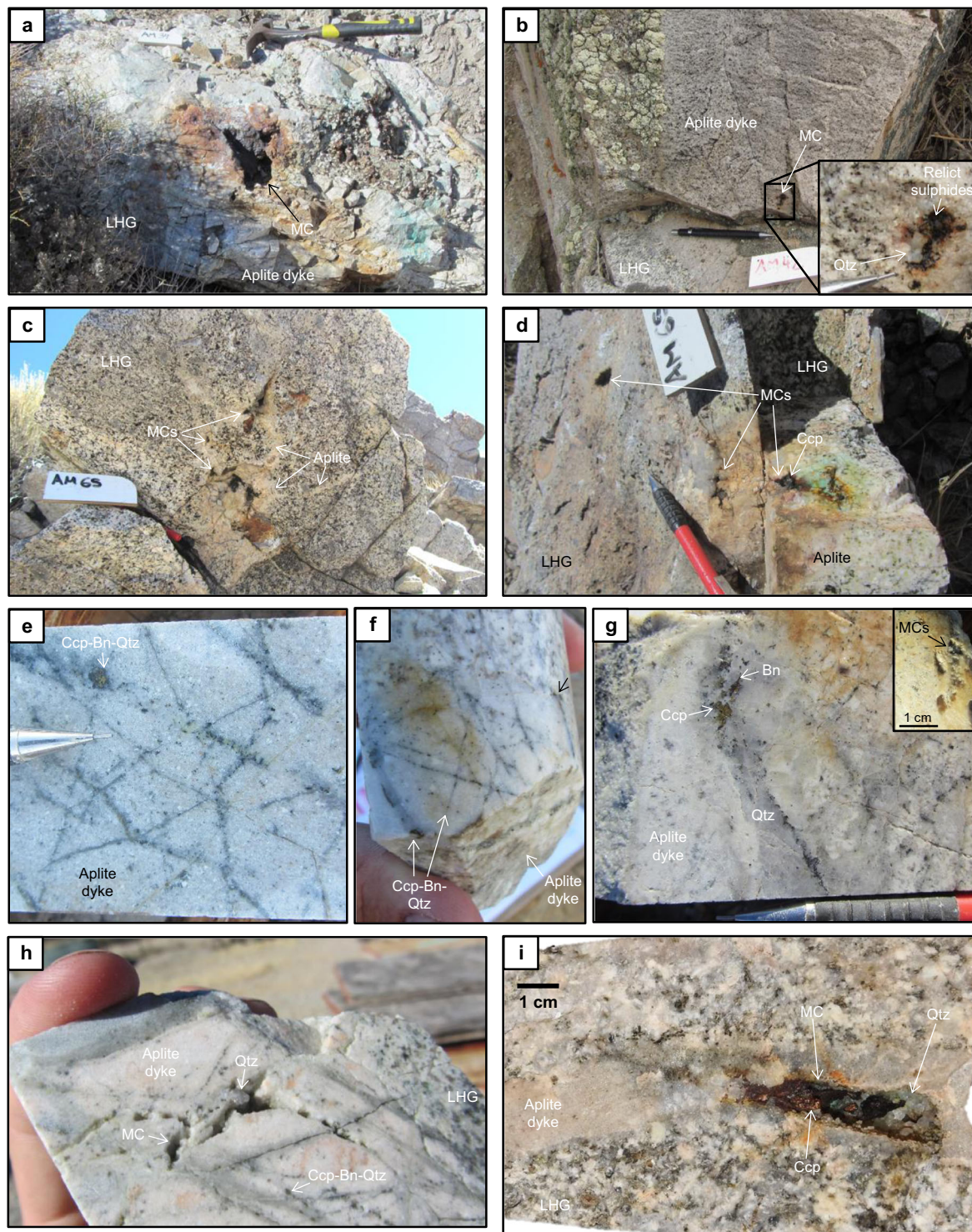
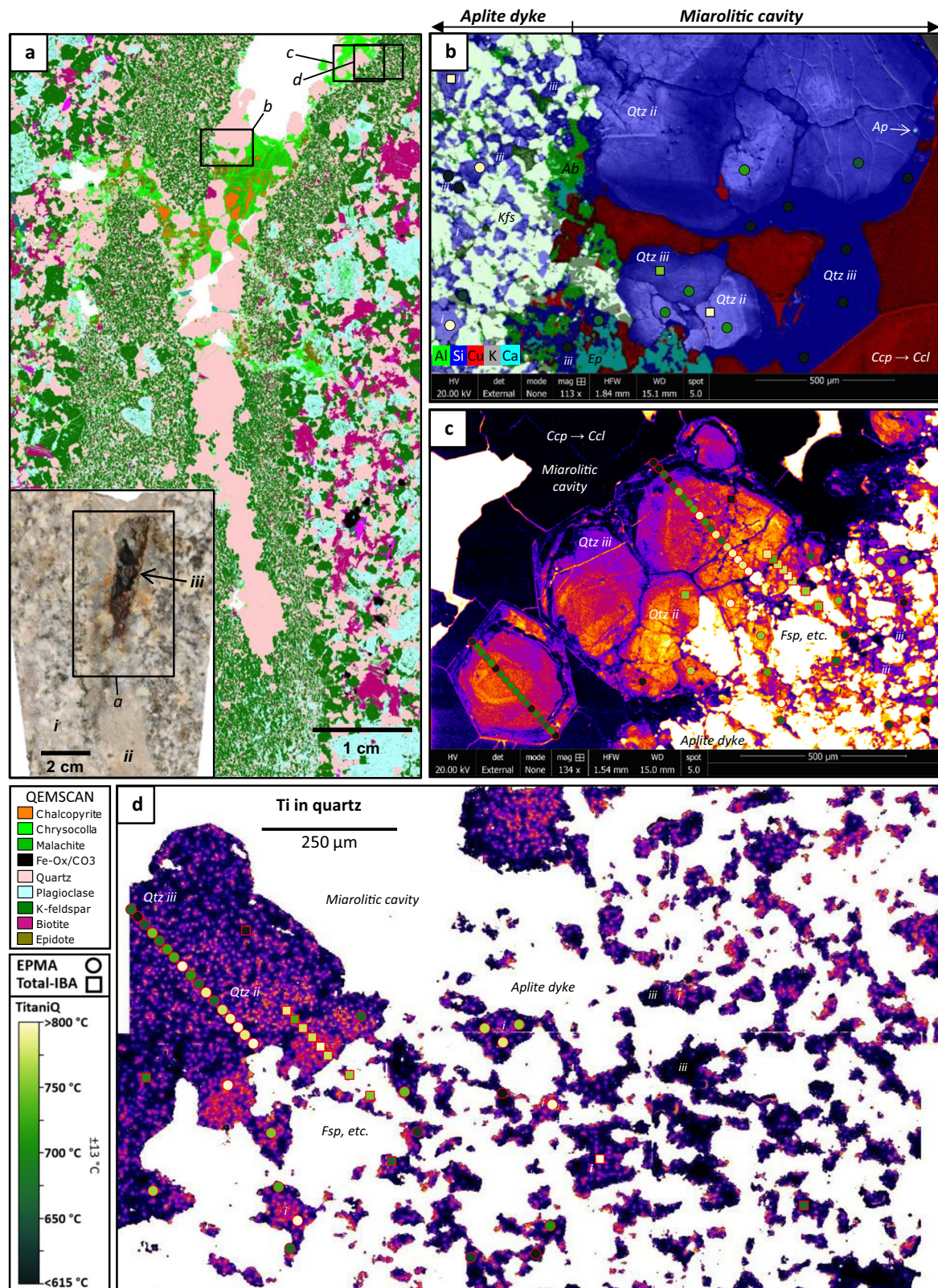


**Fig. 4 Fluid exsolution and mineralisation in aplite dykes. a-d** Field photographs of miarolitic cavities (MCs) within aplite dykes, some mineralised with chalcopyrite (Ccp), which is undoubted textural evidence for mineralising fluid exsolution<sup>27</sup>. The aplite dykes cross-cut the exposed cupola of the Luhr Hill granite (LHG), which, pre-tilting, would have sat beneath the Ann Mason porphyry deposit<sup>14</sup>. Qtz = quartz. Hammer and pencil for scale; **e, f** Drill core from the Ann Mason porphyry deposit showing aplite dykes hosting early chalcopyrite-bornite (Bn)-quartz (A-type, nomenclature after<sup>44</sup>) veins, locally terminating at dyke margins (black arrow in **f**). Pencil and thumb for scale; **g** Drill core from the Ann Mason porphyry deposit showing a mineralised aplite dyke. Pencil for scale. Inset, miarolitic cavity on the backside of this sample; **h** Drill core from the Ann Mason porphyry deposit showing an aplite dyke hosting mineralised miarolitic cavities closely associated with early chalcopyrite-bornite-quartz (A-type, nomenclature after<sup>44</sup>) veins. Finger for scale; **i** Sample from the exposed cupola of the Luhr Hill granite showing the granite cut by an aplite dyke hosting a chalcopyrite mineralised miarolitic cavity. Quartz and chalcopyrite clearly crystallised into open space, with euhedral crystal shapes and terminations. This sample is the focus of Fig. 5.



we interpret the hypogene copper mineralisation (mostly chalcopyrite) to be associated with hydrothermal fluids that formed the relatively late branching, interconnected quartz ('Qtz iii' in Fig. 5b–d and 6). Thus, the wormy quartz texture records the pathways of mineralising hydrothermal fluids between earlier crystallised quartz and feldspars (and accessory phases). The flow

of these fluids caused the partial dissolution of earlier quartz, seen as resorbed margins (Figs. 5b, c and 6), broadening the pathways and exaggerating the wormy texture. It should be noted that, because of this addition of hydrothermal quartz in the aplites, quartz proportions, relative to K-feldspar and plagioclase, will be over reported. This will affect the interpretation of petrological

**Fig. 5 Mineralising aplitic mush at the magmatic-hydrothermal transition.** **a** QEMSCAN mineral map and field photograph (inset) of the Luhr Hill granite (i) cut by an aplite dyke (ii) which hosts hypogene Cu-mineralised miarolitic cavities (iii) (boxes show location of **b**, **c**, **d**); **b** SEM-CL image overlain by SEM-EDX elemental map of the aplite dyke and miarolitic cavity showing the locations of EPMA (circles) and Total-IBA analyses (squares) for crystallisation temperature estimates using TitaniQ<sup>39</sup>. Distinct quartz (Qtz) generations are shown in different shades of blue (*i*, *ii* and *iii*) and chalcopyrite (Ccp) altering to chrysocolla (Ccl) in red. In the aplite, albite (green, Ab) is mostly associated with K-feldspar (light green, Kfs) as lamellae within and as individual grains. Quartz is paragenetically late in the aplite, containing few inclusions of albite and K-feldspar, being either intergranular (blocky) 'bright' CL 'Qtz *i*' ( $T > 720$  °C), or forming branching interconnected networks comprising hydrothermal zoned 'Qtz *ii*' and increasingly 'darker' CL 'Qtz *iii*' ( $T < 700$  °C). Copper-bearing phases (Ccp and Ccl) appear mostly associated with 'Qtz *iii*'. Resorbed margins can be seen in all quartz generations. Ap = apatite, Ep = epidote; **c** False colour SEM-CL image (symbols as in **b**) showing branching interconnected 'Qtz *ii* & *iii*' joining the miarolitic cavity. Non-quartz phases appear white or black. Fsp = feldspar; **d** Total-IBA map of Ti concentrations in quartz (symbols as in **b**). All other phases appear white. Higher Ti 'Qtz *i*' (yellow-orange) is present as inclusions in feldspars. Lower Ti 'Qtz *ii*' (orange-purple) and 'iii' (purple-black) quartz occur as branching networks between all other phases.

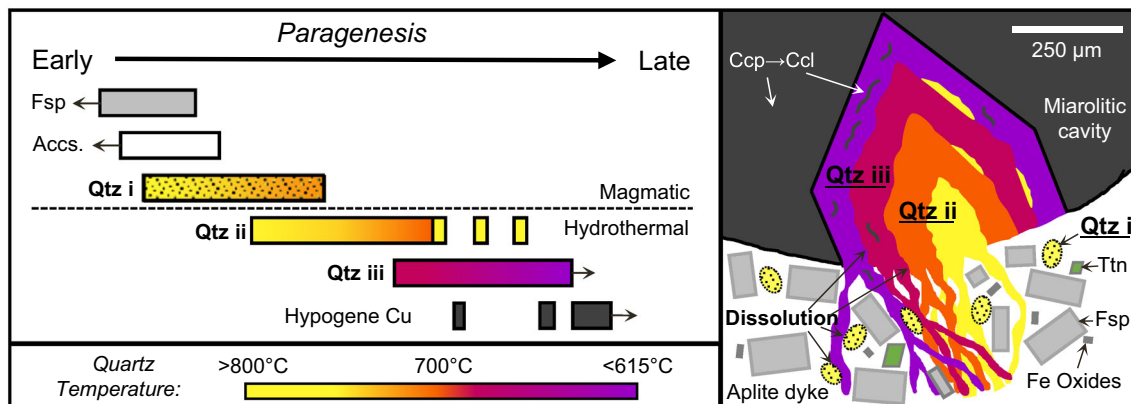


**Fig. 6 Timing and temperature of crystallisation in aplite crystal mush dykes.** Summary paragenetic diagram and sketch showing the spatial, temporal and temperature relations between magmatic phases in the crystal mush framework (comprising feldspars [Fsp], 'Qtz *i*' and accessory phases such as titanite [Ttn]), mineralised miarolitic cavities and the late wormy quartz ('Qtz *ii* & *iii*') network which marks palaeoporosity. The hydrothermal fluids flowed through the mush's inter-crystal spaces to reach miarolitic cavities and to form veins. These fluids continued to flow after the miarolitic cavities formed, evidenced by the 'Qtz *ii* & *iii*' generations progressively filling the miarolitic cavities and partly resorbing earlier quartz generations. Repeated pulses of fluid flow are evidenced from the quartz within the miarolitic cavity, with 'Qtz *iii*' containing inclusions of slightly higher temperature 'Qtz *ii*'. Quartz generations are coloured as per their CL response and titanium concentration in Fig. 5c, d. Hypogene Cu mineralisation (Chalcopyrite [Ccp], locally altered to secondary chrysocolla [Ccl]), is associated with the later quartz generations. Temperatures are approximate, based on ranges from our TitaniQ<sup>39</sup> thermometry.

and geochemical data, mainly diluting the concentrations of other phases and components, not only for the aplites described herein but also in other rock types infiltrated by hydrothermal fluids.

Due to the presence of these inter-crystal (mush) pathways, mineralising hydrothermal fluids could have continuously migrated upwards through the aplite dykes from an underlying large-volume parent intrusive which had reached fluid saturation (i.e., the evolved internal regions of the Luhr Hill granite), until hydrothermal quartz sealed the inter-crystal spaces (represented by the branching 'Qtz *ii* & *iii*' generations; Figs. 5 and 6). As such, the pervasive aplite dykes acted as conduits, we suggest the term "crystal mush dykes", for the upward transport and focusing of the large volumes of mineralising hydrothermal fluids necessary to create the porphyry deposits (Fig. 7). We envisage the following sequence for the formation of the crystal mush dykes and their role in the transport and focusing of porphyry-forming fluids: (1) The incremental emplacement of the multi-pluton Yerington batholith into the shallow crust involving increasingly more evolved magmas<sup>14</sup> (Fig. 1); (2) Inward crystallisation of the undercooled Luhr Hill granite and fracturing of the crystalline carapace, probably due to tectonic activity<sup>9</sup> (Fig. 7); (3) Upward emplacement of granitic magmas to form numerous generations of porphyry and aplite dykes (TitaniQ<sup>39</sup> > ~720 °C); (4) Cessation of magma flow and crystallisation within the aplite dykes during periods of rapid pressure changes and undercooling, to form UST pegmatites<sup>28</sup> (Fig. 3), and fluid exsolution to produce miarolitic

cavities<sup>27</sup> (TitaniQ<sup>39</sup> ~775–700 °C) (Figs. 4 and 5); (5) Penecontemporaneous formation of a crystal mush in the aplite dykes, at the magmatic-hydrothermal transition, due to the last remaining vestiges of interstitial liquid consisting of aqueous fluid (Fig. 6); (6) Upward transport of pressurized fluids to the shallow porphyry environment through inter-crystal pathways in the mush dykes from extensive volumes of underlying fluid-saturated magmas (Luhr Hill granite) (Figs. 6 and 7); (7) Fluid pressure increase, due to upward fluid transport and accumulation, reducing effective stress<sup>48</sup>, to trigger brittle failure of the wall rocks and subsequent formation of A- and, in turn, B-type veins (nomenclature after<sup>44</sup>), with an associated pressure drop. Once formed, the hydrothermal veins could have acted as the classic fluid pathways through the upper portions of the porphyry system; (8) Porphyry-style disseminated and vein-type mineralisation in a narrow zone to form porphyry deposits; (9) Sealing of porosity in the mush dyke due to cooling and/or depressurization of the system leading to progressive quartz precipitation within the inter-crystal mush network (represented by the progressive crystallisation of 'Qtz *ii*' to 'iii', with TitaniQ<sup>39</sup> down to <615 °C) (Figs. 5 and 6). Whilst there may be other possible explanations for some aspects of this scheme, because of challenges related to determining the relative timing of different generations of dykes and veins, our textural observations can only suggest and not prove that the granite cupola or large porphyry dykes did not exsolve volatiles.

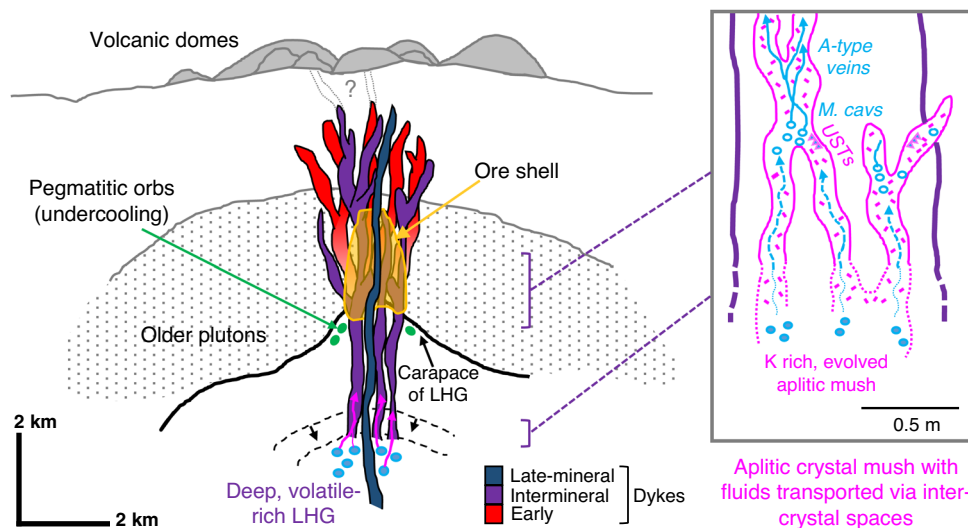


**Fig. 7 Crystal mush dykes acting as fluid conduits.** Schematic cross-section (modified after<sup>5</sup>) through the Yerington porphyry system showing emplacement of a series of older plutons, the undercooled Luhr Hill granite (LHG), with a crystalline carapace, and multiple generations of porphyry and aplite dykes. Quartz unidirectional solidification textures (USTs) in the aplite dykes likely resulted from rapid pressure fluctuations<sup>28</sup> and fluid exsolution via first-type boiling<sup>40</sup>. Crystallisation of the aplitic melts led to formation of a magmatic crystal mush framework and, with fluid exsolution, miarolitic cavities (M. cavs). The aplitic crystal mush dykes continued to act as conduits for the upward flow of pressurized mineralising fluids via their inter-crystal spaces from evolved, deep portions of the Luhr Hill granite. The resultant increase in fluid pressure triggered hydro-fracturing to allow the formation of A- and, in turn, B-type veins (nomenclature after<sup>44</sup>).

We conclude that, within the Yerington District, the roof zone of the Luhr Hill granite and its apophyses was a carapace rather than a mineralising cupola. It was the aplite dykes reaching water saturation and providing mush conduits for fluid flow from deeper within the magmatic system which provided the large volumes of hydrothermal fluid necessary for porphyry deposit formation, as magma and volatile transport were de-coupled. In determining this, we have presented some of the first petrographic field and microscale evidence for the occurrence of magmatic-hydrothermal mush, and highlighted the development and the potential importance of crystal mush dykes in the formation of porphyry copper deposits. Their development can explain how large volumes of magmatic-hydrothermal fluids can be extracted and focused from extensive regions of magmatic systems. This is consistent with geochronological evidence from other porphyry occurrences that hydrothermal systems are not linked to the lifetime of porphyry intrusions e.g.<sup>49</sup>. This was difficult to reconcile when cupolas were thought to be the direct source of fluids e.g.<sup>4,5,11,15–17,20–22</sup>, mainly given the paucity of geophysical evidence for crystal-poor bodies of large volume in the shallow crust e.g.<sup>50</sup>. The new constraints our findings place on the temporal and spatial nature of fluid exsolution and migration will help in the further development of exploration and numerical models for porphyry-style deposits. In addition to this, the recognition of hydrothermal quartz within an aplite dyke, which would have been considered by most workers to be entirely magmatic in origin, may influence the interpretation of mineralogical and geochemical data for a wide variety of rocks formed at the magmatic-hydrothermal transition, e.g., Sn-W granitic systems e.g.<sup>51</sup>. Our findings also have significance for the interpretation and forecasting of volcanic processes since dykes are important feeders of volcanic edifices. The possibility that a separate fluid phase can be transported through dykes, with increasing fluid pressure reducing effective stress (therefore rock strength and ductility)<sup>48</sup>, is likely to have major implications for degassing and in determining volcanic stability and explosivity.

## Methods

The fundamental first-order controls for this study were from field observations of cross-cutting relationships, disequilibrium phenomena and textures indicative of fluid exsolution from outcrop across the Yerington District and drillcore from the Ann Mason and Yerington porphyry copper deposits.

**Scanning electron microscopy.** Selected samples were prepared as polished uncovered thin sections (30  $\mu\text{m}$  thickness) at Camborne School of Mines, University of Exeter, UK. Following optical microscopy, section surfaces were carbon coated to a thickness of 25 nm using an Emitech K950 carbon coater. Scanning electron microscope (SEM) backscattered electron (BSE) and cathodoluminescence (CL) imaging alongside and qualitative energy dispersive X-ray (EDX) elemental mapping were carried out using an FEI Quanta 650 FEG-SEM equipped with a Gatan monochrome CL detector and 2x Bruker SDD EDS detectors (XFlash series 6 | 30) at the University of Exeter's Environment and Sustainability Institute. The instrument was operated at an accelerating voltage of 20 kV. Elemental maps were obtained using a minimum of 4 scans and a dwell time of 32  $\mu\text{s}$ , and processed using Bruker Esprit software version 1.9a. The CL images were collected from single scans with a 30  $\mu\text{s}$  dwell time, a processing resolution of 3072  $\times$  2048 pixels and 256 grey levels. CL brightness and contrast were optimized to reveal inhomogeneities in quartz, other phases therefore appear either white or black.

In the SEM-CL images, the different grey levels shown by quartz represent different luminescence colours that can be attributed to defects in the lattice and/or the presence of trace elements in the crystal structure<sup>52</sup>. Selected images were retrospectively false-coloured using a 'fire' look-up table, using ImageJ software, to visually intensify differences in CL response from different quartz generations.

The mineralogy of sample AM13 (sample details in Supplementary Data 1) was determined using a QEMSCAN 4300 automated mineralogical assessment system at Camborne School of Mines<sup>53–55</sup>. The system is based on a Zeiss Evo 50 SEM with 4x Bruker SDD EDS detectors (XFlash) controlled by iMeasure v. 4.2SR1 software for data acquisition and iDiscover v. 4.2SR1 and 4.3 for spectral interpretation and data processing<sup>56</sup>. The same 30  $\mu\text{m}$  thick carbon-coated polished thin section was used for the SEM studies. The QEMSCAN was operated at an accelerating voltage of 25 kV and a beam current of 5 nA, with a working distance of around 22 mm, in high vacuum mode and with automatic beam calibration every 30 min. Fieldscan measurement mode was used to obtain a mineralogical map of nearly the whole polished section area (39  $\times$  20 mm) at an analytical point resolution, or pixel spacing, of 10  $\mu\text{m}$  and with 1000 X-ray counts per pixel. The data from each point of analysis was automatically compared with a Species Identification Protocol (SIP) database of mineral and noncrystalline phase spectra to identify the minerals present. The SIP used was modified from the LCU5 SIP provided with the QEMSCAN, which includes a range of oxide, sulfate, and silicate minerals. All mineral categories were checked by manually assessing elemental abundances, element ratios, and BSE signal. A boundary phase post processor was applied to improve edge effects and to resolve rogue pixels. Data collection and processing followed in house QA/QC procedures. The data were



output as mineralogical maps (Fig. 4a, Supplementary Data 2) and in a mineral associations matrix (Supplementary Data 2).

**Electron probe microanalysis (EPMA).** Concentrations of Al, Ti and Fe in quartz were determined by EPMA using a JEOL JXA-8200 electron microprobe at Camborne School of Mines, University of Exeter. The thin sections used for the SEM studies were re-polished and carbon coated to a thickness of 25 nm in an Emitech K950 carbon coater. The instrument was operated at an accelerating voltage of 20 kV, a beam current of 70 nA and a spot size of 15  $\mu\text{m}$ . This relatively large spot size was used due to the sensitivity of quartz at high current under a narrow beam<sup>57</sup>.  $\text{SiO}_2$  was assumed to be 100%. Corundum (Geo MkII), rutile and hematite (Astimex) calibration standards were used for Al, Ti and Fe, respectively. For calibration at low concentrations or as ‘blank’-control, some studies use a synthetic doped or pure  $\text{SiO}_2$ -glass. This was deemed inappropriate as their behaviour during electron irradiation is very different to that of quartz e.g.<sup>57</sup>. Peak and background measurement count times were both 200 s. Limits of detection (LOD) were  $(2\sigma)$  30 ppm for Al, 28 ppm for Ti and 28 ppm for Fe. To estimate precision, we undertook 7 repeat analyses of a single homogenous, magmatic, unzoned (from SEM-CL imaging) quartz crystal from within a polished section of Luhr Hill granite (sample YM33b in Supplementary Data 1). The mean; ranging from; half of the range; 1 S.D. of these were: Al (78; 51–101; 25; 20 ppm); Ti (81; 70–91; 10; 8 ppm); Fe (39; 28–52; 12; 12 ppm). From these we use  $\pm 1$  S.D. to determine our analytical uncertainties: Al  $\pm 20$  ppm; Ti  $\pm 8$  ppm; Fe  $\pm 12$  ppm.

**Total Ion Beam Analysis (Total-IBA).** Total-IBA, to determine trace elements in quartz from a selected thin section (AM13, sample details in Supplementary Data 1), was performed using the microbeam line on the 2MV Tandemron accelerator (HVEE Corporation, NL) installed at the University of Surrey Ion Beam Centre. The same thin section as for the SEM and EPMA studies was used, but prior to analysis was re-polished and carbon coated to a thickness of 25 nm using an Emitech K950 carbon coater. The experiments reported here were carried out using a 2.5 MeV proton beam, focused to a diameter of 2  $\mu\text{m}$  with a beam current between 700 and 1000 pA, measured in a spectroscopically pure graphite Faraday cup mounted behind the samples. The X-rays were detected using a lithium drifted silicon detector with an active area of 80  $\text{mm}^2$  mounted at a central angle of 135° to the beam direction in the horizontal plane. The X-ray detector was fitted with a 130  $\mu\text{m}$  beryllium foil absorber and a 30 or 75  $\mu\text{m}$  (experiment dependent) Kapton foil. The beryllium foil is used routinely to avoid spectral degradation due to backscattered particles entering the detector, and the additional Kapton foil was used to attenuate the spurious escape peak from the intense K $\alpha$  line of potassium in the K-feldspar regions of the sample which interferes with the Si K $\alpha$  line. Elastically backscattered protons (EBS) were detected using a PIPS charged particle detector with an active area of 300  $\text{mm}^2$  mounted 52 mm from the sample at a central angle of 128° to the beam direction in the vertical plane. Data were acquired using the OMDAQ-3 software package (Oxford Microbeams Ltd., UK, [www.microbeams.co.uk](http://www.microbeams.co.uk)). 6 adjacent 500  $\times$  500  $\mu\text{m}$  areas were qualitatively mapped until 3400 nC of charge were reached, and the maps subsequently stitched together. Quantitative analyses of selected points were acquired until 100 nC of charge were reached.

Particle-induced X-ray emission (PIXE) spectra were quantified using the OMDAQ-3 interface to GUPIX<sup>58</sup>. GUPIX applies corrections based on the composition of the local sample matrix obtained by processing the associated EBS spectrum<sup>59</sup>. This employs an algorithm implemented in OMDAQ-3 which uses non-Rutherford proton elastic scattering cross sections obtained from the IBANDL database<sup>60</sup> maintained by the International Atomic Energy Agency. The only instrumental calibration routinely required is to determine variation of X-ray detector efficiency with energy. This is achieved by analysing a lead-glass standard reference material (BCR-126A, European Commission, Joint Research Centre (JRC), Geel, Belgium), and adjusting the parameters in the model of the efficiency to optimize the accuracy of determination for all detected elements<sup>61</sup>. For these measurements the relative standard deviation of measured concentration from the certified values of major elements in the standard glass was 5%. The thick Kapton filter used to suppress the K K $\alpha$  X-ray lines introduces a significant uncertainty into the Si determination and so concentrations were normalised by scaling the PIXE concentration for Si to the concentrations determined by EBS. Results, limits of detection and analytical uncertainty are presented in Supplementary Data 1.

To generate a Ti-in-quartz map, all non-quartz phases (i.e., anything containing Al, Ca, Cu, Fe, or K as a major element) were filtered out (rendered white) using ImageJ software. The resulting Ti-in-quartz map was then false coloured using a ‘fire’ look-up table for direct visual comparison with similarly false coloured SEM-CL images.

**TitaniQ geothermometry.** The TitaniQ geothermometer<sup>39</sup> (Eq. 1) was used to assess the crystallisation temperatures of different generations of quartz. Ti concentrations were determined by EPMA and Total-IBA spot analyses (see above). TitaniQ has been shown to be affective for crystallisation temperatures of between 600 °C and 1000 °C, at 10 kbar<sup>39</sup>. Whether and how TitaniQ can be applied at other pressures has been strongly debated e.g.<sup>62–64</sup>. It is reported that there was little temperature effect on Si-Ti interdiffusion, i.e., on temperatures derived from TitaniQ, between experiments carried out at 1 atm<sup>65</sup> and those predicted at 10 kbar<sup>39</sup>.

In addition to this, there is general agreement that calculated temperatures vary little across the limited 1–3 kbar pressure range typical of the porphyry environment e.g.<sup>20</sup>. As such, the TitaniQ method was deemed appropriate for use in the current study without applying a pressure correction. The activity of  $\text{TiO}_2$  ( $a_{\text{TiO}_2}$ ) was assigned a value of 0.7 based on estimates from thermodynamic modelling of felsic magmas<sup>66</sup>, previous work on other felsic magmatic systems e.g.<sup>67,68</sup> and specific studies on the Yerington District<sup>69</sup>. We acknowledge that the  $a_{\text{TiO}_2}$  may have changed during the crystallisation history and evolution of the magmatic system, but assume that this was negligible given that the same Ti-bearing minerals (notably titanite and trace rutile, see Supplementary Data 2) are present in the compositionally similar granite and aplite dykes which are the focus of the current study. At  $\sim 700$  °C, an increase in  $a_{\text{TiO}_2}$  of 0.1 would decrease the calculated temperature by only 13 °C, and a decrease in  $a_{\text{TiO}_2}$  of 0.1 would increase the temperature by only 17 °C. To estimate precision, we calculated TitaniQ for 7 repeat EPMA analyses of a single homogenous, magmatic, un-zoned quartz phase within the Luhr Hill granite (sample YM33b in Supplementary Data 1). These give a mean of 765 °C, ranging from 748 to 779 °C, with half the range being 16 °C and 1 S.D. of 13 °C. For Total-IBA, analytical uncertainty for individual analyses are typically less than those for EPMA (Supplementary Data 1) and therefore yield TitaniQ calculation uncertainties less than those for EPMA analyses described above. We therefore use 1 S.D. of the repeated EPMA analyses to determine our analytical uncertainty of  $\pm 13$  °C.

$$T_{\text{Ti-quartz}} (\text{°C}) = \frac{-3765}{\log\left(\frac{x_{\text{Ti}}^{\text{qtz}}}{a_{\text{TiO}_2}}\right) - 5.69} - 273 \quad (1)$$

where  $x_{\text{Ti}}^{\text{qtz}}$  is the Ti concentration in quartz and  $a_{\text{TiO}_2}$  is the activity of  $\text{TiO}_2$  in the system.

## Data availability

The authors declare that the data supporting the findings of this study are available within the paper and its Supplementary Information files. QEMSCAN, EPMA and Total-IBA data are also available at <https://doi.org/10.5281/zenodo.4482715>.

Received: 19 August 2020; Accepted: 16 February 2021;

Published online: 17 March 2021

## References

- Cline, J. S. & Bodnar, R. J. Can economic porphyry copper mineralization be generated by a typical calc-alkaline melt? *J. Geophys. Res.* **96**, 8113–8126 (1991).
- Buret, Y. et al. From a long-lived upper-crustal magma chamber to rapid porphyry copper emplacement: reading the geochemistry of zircon crystals at Bajo de la Alumbrera (NW Argentina). *Earth Planet. Sci. Lett.* **450**, 120–131 (2016).
- Tapster, S. et al. Rapid thermal rejuvenation of high-crystallinity magma linked to porphyry copper deposit formation; evidence from the Koloula Porphyry Prospect, Solomon Islands. *Earth Planet. Sci. Lett.* **442**, 206–217 (2016).
- Richards, J. P. Cumulative factors in the generation of giant calc-alkaline porphyry Cu deposits. In: *Super Porphyry Copper and Gold Deposits: A Global Perspective*, v. 1 (ed. Porter, T. M.) 7–25 (Adelaide, PGC Publishing, 2005).
- Sillitoe, R. H. Porphyry copper systems. *Econ. Geol.* **105**, 3–41 (2010).
- Cashman, K. V., Stephen, R. J. & Blundy, J. D. Vertically extensive and unstable magma systems: a unified view of igneous processes. *Science* **355**, 6331 (2017).
- Sparks, R. S. J. & Cashman, K. V. Dynamic magma systems: implications for forecasting volcanic activity. *Elements* **13**, 35–40 (2017).
- Jackson, M. D., Blundy, J. & Sparks, R. S. J. Chemical differentiation, cold storage and remobilization of magma in the Earth’s crust. *Nature* **564**, 405–409 (2018).
- Richards, J. P. A shake-up in the porphyry world? *Econ. Geol.* **113**, 1125–1233 (2018).
- Seedorff, E., Barton, M. D., Stavast, W. J. A. & Maher, D. J. Root zones of porphyry systems: extending the porphyry model to depth. *Econ. Geol.* **103**, 939–956 (2008).
- Weis, P., Driesner, T. & Heinrich, C. A. Porphyry-copper ore shells form at stable pressure-temperature fronts within dynamic fluid plumes. *Science* **338**, 1613–1616 (2012).
- Wilkinson, J. J. Triggers for the formation of porphyry deposits in magmatic arcs. *Nature Geoscience* **6**, 917–925 (2013).
- Richards, J. P. Clues to hidden copper deposits. *Nature Geoscience* **9**, 195–196 (2016).
- Dilles, J. H. Petrology of the Yerington Batholith, Nevada: evidence for evolution of porphyry copper ore fluids. *Econ. Geol.* **82**, 1750–1789 (1987).
- Candela, P. A. Physics of aqueous phase evolution in plutonic environments. *American Mineralogist* **76**, 1081–1091 (1991).

16. Shinohara, H., Kazahaya, K. & Lowenstern, J. B. Volatile transport in a convecting magma column: Implications for porphyry Mo mineralization. *Geology* **23**, 1091–1094 (1995).
17. Cloos, M. Bubbling magma chambers, cupolas, and porphyry copper deposits. *International Geology Review* **43**, 285–311 (2001).
18. Proffett, J. M. Geology of the Bajo de la Alumbrera porphyry copper-gold deposit, Argentina. *Econ. Geol.* **98**, 1535–1574 (2003).
19. Pistone, M. et al. Felsic melt and gas mobilization during magma solidification: An experimental study at 1.1 kbar. *Front. Earth Sci.* **8**, 175 (2020).
20. Seedorff, E. et al. Porphyry deposits: characteristics and origin of hypogene features. *Econ. Geol.* **100**, 251–298 (2005).
21. Corbett, G. Anatomy of porphyry-related Au-Cu-Ag-Mo mineralised systems: Some exploration implications. *AIIG Bull.* **49**, 33–46 (2009).
22. Schöpa, A., Annen, C., Dilles, J. H., Sparks, R. S. J. & Blundy, J. D. Magma emplacement rates and porphyry copper deposits: Thermal modeling of the Yerington Batholith, Nevada. *Econ. Geol.* **112**, 1653–1672 (2017).
23. Bryan, R. C. NI 43-101 Technical Report Mineral Resource Update Yerington Copper Project Lyon County, Nevada. <https://quaterra.com/projects/quateras-yerington-copper-projects/yerington-deposit/>. (2014).
24. Henderson, M. R., Byan, R. C., Welhener, H. E., Jolk, R. W. & Willow, M. A. MacArthur Copper Project; Amended NI 43-101 Technical Report Preliminary Economic Assessment. *M3 Engineering*. <https://quaterra.com/projects/quateras-yerington-copper-projects/macarthur-copper-deposit/> (2014).
25. Kulla, G. et al. Updated Preliminary Economic Assessment on the Ann Mason Project Nevada, USA. *AmeC Foster Wheeler*. [https://www.miningdataonline.com/reports/Ann\\_Mason\\_PEA\\_03032017.pdf](https://www.miningdataonline.com/reports/Ann_Mason_PEA_03032017.pdf). (2017).
26. Dilles, J. H. & Proffett, J. M. Metallogensis of the Yerington batholith, Nevada. In: *Porphyry Copper Deposits of the American Cordillera*. (eds Pierce, F. W. & Bolm, J. G.) **20**, 306–315 (Arizona Geological Society Digest, 1995).
27. Candela, P. A. A review of shallow, ore-related granites: textures, volatiles, and ore metals. *J. Petrol.* **38**, 1619–1633 (1997).
28. Kirwin, D. J. Unidirectional solidification textures associated with intrusion-related Mongolian mineral deposits. In: *Geodynamics and metallogeny of Mongolia with special emphasis on copper and gold deposits: Society of Economic Geologists-International Association for the Genesis of Ore Deposits Field Trip, 2005: IAGOD Guidebook Series 11*. (eds Seltmann, R., Gerel, O. & Kirwin, D. J.) **63–84** (London, Centre for Russian and Central EurAsian Mineral Studies, Natural History Museum, 2005).
29. Moore, J. G. & Lockwood, J. P. Origin of comb layering and orbicular structure, Sierra Nevada Batholith, California. *GSA Bulletin* **84**, 1–20 (1973).
30. Decitre, S., Gasquet, D. & Marignac, C. Genesis of orbicular granitic rocks from the Ploumanac’h Plutonic Complex (Brittany, France): petrographical, mineralogical and geochemical constraints. *Eur. J. Mineral.* **14**, 715–731 (2002).
31. Grosse, P., Toselli, A. J. & Rossi, J. N. Petrology and geochemistry of the orbicular granitoid of Sierra de Velasco (NW Argentina) and implications for the origin of orbicular rocks. *Geol. Mag.* **147**, 451–468 (2010).
32. Ballhaus, C., Raül, O. C., Fonseca, C. M., Kirchenbauer, M. & Zirner, A. Spheroidal textures in igneous rocks – Textural consequences of H<sub>2</sub>O saturation in basaltic melts. *Geochimica et Cosmochimica Acta* **167**, 241–252 (2015).
33. Lentz, D. R. & Fowler, A. D. A dynamic model for graphic quartz-feldspar intergrowths in granitic pegmatites in the Southwestern Grenville Province. *Canadian Mineralogist* **30**, 571–585 (1992).
34. London, D. & Morgan, G. B. The pegmatite puzzle. *Elements* **8**, 263–268 (2012).
35. Rusiecka, M. K., Bilodeau, M. & Baker, D. R. Quantification of nucleation delay in magmatic systems: experimental and theoretical approach. *Contrib. Mineral. Petrol.* **175**, 47 (2020).
36. Baker, D. R. & Freda, C. Eutectic crystallization in the undercooled Orthoclase-Quartz-H<sub>2</sub>O system: experiments and simulations. *Eur. J. Mineral.* **13**, 453–466 (2001).
37. Fenn, P. M. On the origin of graphic granite. *American Mineralogist* **71**, 325–330 (1986).
38. London, D. The application of experimental petrology to the genesis and crystallisation of granitic pegmatites. *Canadian Mineralogist* **30**, 499–540 (1992).
39. Wark, D. A. & Watson, E. B. TitaniQ: a titanium-in-quartz geothermometer. *Contrib. Mineral. Petrol.* **152**, 743–754 (2006).
40. Candela, P. A. Felsic magmas, volatiles, and metallogenesis. In: *Ore Deposition Associated with Magmas. Reviews in Economic Geology*. (eds Whitney, J. A. & Naldrett, A. J.) 223–233 (1989).
41. Stefanova, E. et al. Melt and fluid inclusions in hydrothermal veins: the magmatic to hydrothermal evolution of the elatsite porphyry Cu-Au deposit, Bulgaria. *Econ. Geol.* **109**, 1359–1381 (2014).
42. Runyon, S. E. et al. Coarse muscovite veins and alteration in porphyry systems. *Ore Geol. Rev.* **113**, 103045 (2019).
43. Chang, J., Li, J. W. & Audétat, A. Formation and evolution of multistage magmatic-hydrothermal fluids at the Yulong porphyry Cu-Mo deposit, eastern Tibet: Insights from LA-ICP-MS analysis of fluid inclusions. *Geochem. Cosmochim. Acta* **232**, 181–205 (2018).
44. Gustafson, L. B. & Hunt, J. P. The porphyry copper deposit at El Salvador, Chile. *Econ. Geol.* **70**, 857–912 (1975).
45. Candela, P. A. & Blevin, P. L. Do some miarolitic granites preserve evidence of magmatic volatile phase permeability? *Econ. Geol.* **90**, 2310–2316 (1995).
46. Holness, M. B. Melt segregation from silicic crystal mushes: a critical appraisal of possible mechanism and their microstructural record. *Contrib. Mineral. Petr.* **173**, 48 (2018).
47. Allaby, M. A *Dictionary of Geology and Earth Sciences* 4th Edn., p. 573 (Oxford University Press, Oxford, 2013).
48. Terzaghi, K. & Peck, R. B. *Soil Mechanics in Engineering Practice* (John Wiley & Sons, New York, 1948).
49. Li, Y., Selby, D., Condon, D. & Tapster, S. Cyclic magmatic-hydrothermal evolution in porphyry systems: high-precision U-Pb and Re-Os geochronology constraints on the tibetan qulong porphyry Cu-Mo deposit. *Econ. Geol.* **112**, 1419–1440 (2017).
50. Miller, D. S. & Smith, R. B. P and S velocity structure of the Yellowstone volcanic field from local earthquake and controlled source tomography. *J. Geophys. Res.* **104**, 15105–15121 (1999).
51. Lehmann, B. Formation of tin ore deposits: A reassessment. *Lithos* <https://doi.org/10.1016/j.lithos.2020.105756> (2020).
52. Muller, A. et al. Trace elements and cathodoluminescence of quartz in stockwork veins of Mongolian porphyry-style deposits. *Miner. Deposita* **45**, 707–727 (2010).
53. Gottlieb, P. et al. Using quantitative electron microscopy for process mineralogy applications. *J. Min. Metals Mat. Soc.* **52**, 24–25 (2000).
54. Goodall, W. R., Scales, P. J. & Butcher, A. R. The use of QEMSCAN and diagnostic leaching in the characterisation of visible gold in complex ores. *Min. Eng.* **18**, 877–886 (2005).
55. Goodall, W. R. & Scales, P. J. An overview of the advantages and disadvantages of the determination of gold mineralogy by automated mineralogy. *Min. Eng.* **20**, 506–517 (2007).
56. Rollinson, G. K. et al. Characterisation of non-sulphide zinc deposits using QEMSCAN®. *Minerals Engineering* **24**, 778–787 (2011).
57. Kronz, A., Van den Kerkhof, A. M. & Müller, A. Analysis of low element concentrations in quartz by electron microprobe. In: *Quartz: Deposits, Mineralogy and Analytics* (eds Götz, J., Möckel, R.) (Springer Geology, Berlin, 2012). [https://doi.org/10.1007/978-3-642-22161-3\\_9](https://doi.org/10.1007/978-3-642-22161-3_9).
58. Campbell, J. L., Boyd, N. L., Grassi, N., Bonnick, P. & Maxwell, J. A. The Guelph PIXE software package IV. *Nucl. Inst. Meth. Phys. Res. Sect. B* **268**, 3356–3363 (2010).
59. Grime, G. W. The “Q factor” method: quantitative microPIXE analysis using RBS normalization. *Nucl. Inst. Meth. Phys. Res. Sect. B: Beam Inter. Mater. Atoms* **109–110**, 170–174 (1996).
60. Abriola, D. et al. Development of a reference database for Ion Beam Analysis and future perspectives. *Nucl. Inst. Meth. Phys. Res. Sect. B-Beam Inter. Mater. Atoms* **269**, 2972–2978 (2011).
61. Gomez-Morilla, I. et al. An evaluation of the accuracy and precision of X-ray microanalysis techniques using BCR-126A glass reference material. *Nucl. Instr. Meth. Phys. Res. Sect. B: Beam Inter. Mater. Atoms* **249**, 897–902 (2006).
62. Thomas, J. B. et al. TitaniQ under pressure: the effect of pressure and temperature on the solubility of Ti in quartz. *Contrib. Mineral. Petrol.* **160**, 743–759 (2010).
63. Huang, R. & Audétat, A. The titanium-in-quartz (TitaniQ) thermobarometer: a critical examination and re-calibration. *Geochem. Cosmochim. Acta* **84**, 75–89 (2012).
64. Wilson, C. J. N., Seward, T. M., Allan, A. S. R., Charlier, B. L. A. & Bello, L. A comment on: ‘TitaniQ under pressure: the effect of pressure and temperature on the solubility of Ti in quartz’, by Jay B. Thomas, E. Bruce Watson, Frank S. Spear, Philip T. Shemella, Saroj K. Nayak and Antonio Lanzirrotti. *Contrib. Mineral. Petrol.* **164**, 359–368 (2012).
65. Cherniak, D. J., Watson, E. B. & Wark, D. A. Ti diffusion in quartz. *Chem. Geo.* **236**, 65–74 (2007).
66. Ghiorso, M. S. & Gualda, A. R. A method for estimating the activity of titania in magmatic liquids from the compositions of coexisting rhombohedral and cubic iron-titanium oxides. *Contrib. Mineral. Petrol.* **165**, 73–81 (2013).
67. Claiborne, L. L., Miller, C. F. & Wooden, J. L. Trace element composition of igneous zircon: a thermal and compositional record of the accumulation and evolution of a large silicic batholith, Spirit Mountain, Nevada. *Contrib. Mineral. Petrol.* **160**, 511–531 (2010).
68. McDowell, S. M., Miller, C. F., Mundil, R., Ferguson, C. A. & Wooden, J. L. Zircon evidence for a ~200 k.y. supereruption-related thermal flare-up in the Miocene southern Black Mountains, western Arizona, USA. *Contrib. Mineral. Petrol.* **168**, 1031 (2014).
69. Dilles, J. H. et al. Zircon compositional evidence for sulfur-degassing from ore-forming arc magmas. *Econ. Geol.* **110**, 241–251 (2015).

## Acknowledgements

The author is supported by a NERC GW4 + Doctoral Training Partnership studentship from the Natural Environment Research Council [NE/L002434/1], with additional support from the British Geological Survey and the Natural History Museum, London. This work is also supported by the NERC Highlight Topic award “From arc magmas to ores (FAMOS): A mineral systems approach” [NE/P017452/1]. The author is thankful for additional funding from the Society of Economic Geologists Foundation’s Hugh McKinstry Fund. D. First, Quaterra Resources and Hudbay Resources (previously Mason Resources) are thanked for introductions, access to drill core and field support. S. Pendray, J. Pickles and J. Anderson (Camborne School of Mines, University of Exeter) are thanked for thin section preparation and EPMA support respectively. The EPSRC UK National Ion Beam Centre (UKNIBC) is thanked for a pump-priming grant for the Total-IBA analysis and V. Palitsin is thanked for assistance with the analysis. R. Her- rington, J. Wilkinson and R. Armstrong (Natural History Museum, London), A. Rust and K. Cashman (University of Bristol), and D. Kirwin are thanked for fruitful proof of concept discussions. A. Müller (Natural History Museum, University of Oslo) is also thanked for critical comments on the manuscript.

## Author contributions

L.C.C., B.J.W. and S.T. performed proof of concept and wrote the manuscript. L.C.C. and B.J.W. performed field studies. L.C.C. carried out petrographic and textural studies, SEM-EDX, SEM-CL and EPMA analyses at Camborne School of Mines. G.K.R. performed QEMSCAN® analyses at Camborne School of Mines and contributed to the manuscript. C.C. and G.W.G. performed Total-IBA analyses at the University of Surrey’s Ion Beam Centre and contributed to the manuscript. L.C.C. prepared the figures.

## Competing interests

The authors declare no competing interests.

## Additional information

**Supplementary information** The online version contains supplementary material available at <https://doi.org/10.1038/s43247-021-00128-4>.

**Correspondence** and requests for materials should be addressed to L.C.C.

**Peer review information** Primary handling editor: Joe Aslin

**Reprints and permission information** is available at <http://www.nature.com/reprints>

**Publisher’s note** Springer Nature remains neutral with regard to jurisdictional claims in published maps and institutional affiliations.



**Open Access** This article is licensed under a Creative Commons Attribution 4.0 International License, which permits use, sharing, adaptation, distribution and reproduction in any medium or format, as long as you give appropriate credit to the original author(s) and the source, provide a link to the Creative Commons license, and indicate if changes were made. The images or other third party material in this article are included in the article’s Creative Commons license, unless indicated otherwise in a credit line to the material. If material is not included in the article’s Creative Commons license and your intended use is not permitted by statutory regulation or exceeds the permitted use, you will need to obtain permission directly from the copyright holder. To view a copy of this license, visit <http://creativecommons.org/licenses/by/4.0/>.

© The Author(s) 2021